ORIGINAL PAPER

Effect of vanadium on hydrogen embrittlement susceptibility of high-strength hot-stamped steel

Wei-jian Chen[1,2] · Peng-fei Gao[1,2] · Shuai Wang[1,2] · Hong-zhou Lu[3] · Zheng-zhi Zhao[1,2]

Abstract

Based on the chemical composition of traditional hot-stamped steel (e.g., 22MnB5 and 30MnB5), Nb and V microalloying elements are added into 30MnB5 steel to meet the requirements of ultra-high strength, excellent ductility and potent resistance to hydrogen embrittlement (HE) at the same time. The influence of hot-stamped steel on HE was studied by conducting a hydrogen permeation method and pre-charged hydrogen slow strain rate test. Meanwhile, the experimental steel microstructures and corresponding fracture surfaces are observed and analyzed to characterize HE behavior. The results show that a finer microstructure, a lower apparent diffusion coefficient of hydrogen and a smaller percentage of strength and plasticity reduction are obtained due to the addition of the vanadium element into hot-stamped steel. Compared to the V free experimental steel, the steel with 0.14 wt.% V has a large number of dispersive precipitates and more grain boundary areas, which makes hydrogen atoms dispersedly distribute.

Keywords Hot-stamped steel · Vanadium · Hydrogen embrittlement · Hydrogen permeation test · Slow strain rate test · Microstructure

1 Introduction

With the increasing global production and sales of automobiles, the development of automobile steel is entering the generation of high-strength martensitic steel and quenching–partitioning (Q&P) steel. In order to meet this trend, we are moving toward a new generation of high-quality automotive steel with higher strength and better formability to meet stricter environmental standards and safety requirements. However, as the strength of automobile steel increases, it inevitably faces problems such as delayed fracture of hydrogen and deteriorative quality of stamped parts. When the strength of component materials is more than 1000 MPa, the traditional cold stamping technology

shows a lot of shortcomings in the forming process of the ultra-high-strength steel plate. Therefore, the high-strength hot-stamping technology has emerged. Compared with cold stamping technology, hot stamping technology has many advantages: good ductility in the forming process, and possibility to manufacture complex and high size accuracy parts without springback [1–4].

Although hydrogen embrittlement (HE) behaviors of high-strength steel have been intensively investigated [5–10], no consensus about the basic HE mechanism has been reached. Among them, the role of precipitates (type, size, quantity, etc.) in high-strength steel is quite complicated. Han et al. [11] used TiC precipitated particles to inhibit austenite grain growth and enlarge dislocation density simultaneously in the process of heating and quenching, which resulted in dislocation strengthening and then the increased strength and toughness of the steel. Cai et al. [12] found that Mo and Nb play the role of nanometer precipitation strengthening in the steel, and the solution of Nb in austenite could improve the solubility of C, while Mo could strengthen the effect of C and Nb could stabilize austenite and delay the precipitation of Nb(C, N), which led to the increase in retained austenite volume fraction and mechanical stability in the steel, thereby increasing the yield strength and

✉ Zheng-zhi Zhao
ustbzzz@126.com

1   Collaborative Innovation Center of Steel Technology, University of Science and Technology Beijing, Beijing 100083, China

2   Beijing Laboratory for Modern Transportation Advanced Metal Materials and Processing Technology, University of Science and Technology Beijing, Beijing 100083, China

3   CITIC Metal Co., Ltd., Beijing 100004, China

toughness of the steel. Zhang et al. [13] studied the effect of different Nb contents on hydrogen-induced delayed cracking of high-strength hot-stamped steel. The results showed that when the steel contains high concentration of hydrogen, the maximum delayed fracture resistance is obtained at a Nb content of 0.053%. With regard to the effect of VC on the capture of hydrogen, Chen et al. [14] charged a ferritic steel with deuterium by means of electrolytic loading to achieve a high hydrogen concentration and then immobilized it in the microstructure with a cryogenic transfer protocol before atom probe tomography (APT) analysis. It could be seen that the hydrogen atoms tend to concentrate in the area where VC particles accumulate, directly indicating that VC particles have a strong ability to trap hydrogen atoms.

In the present work, the purpose of adding microalloying elements into the traditional chemical composition system of hot-stamped steel (e.g., 22MnB5 and 30MnB5) is to reduce the size of austenite and enhance the strength of matrix before martensitic transformation, and a fine martensitic lath will be obtained ultimately after hot-stamping process [15–19]. Compared with V free hot-stamped steel, the vanadium microalloying element is introduced in 30MnBNb hot-stamped steel, the susceptibility to HE and the microstructures are analyzed, and the results are summarized in this paper.

2 Experimental details

2.1 Materials

The chemical composition of the investigated materials is shown in Table 1. Thereinto, V free steel is a comparative steel and 0.14 V steel is a vanadium-containing steel. The experimental steels were smelted in a 25-kg medium-frequency vacuum induction furnace and cast into ingots, which were forged into forged billets with a specification of 40 mm × 100 mm × 100 mm. On the forged billet, ϕ4 mm × 10 mm cylindrical bar specimens were cut and intercepted by mechanical wire cutting. According to the standard YBT5127-1993 "Critical point determination method of steel (expansion method)", the phase transition points of the experimental steels were measured using the German DIL805A thermal expansion instrument as shown

in Table 1. The forged billets were heated and homogenized at 1200 °C for 1 h, then hot rolled to a thickness of 6 mm by 5 rolling passes with a finishing temperature of 870 °C and water cooled to a temperature of 660 °C for 1 h to simulate coiling, followed by furnace-cooling to room temperature. After pickling, the hot-rolled sheets were directly cold rolled to about 1.5 mm in thickness with the cold rolling reduction rate of about 75%.

According to phase transformation points of the experimental steels, heat treatment experiments were carried out and the schematic diagram of the hot-stamping process is presented in Fig. 1. The specimens were heated to the austenitizing temperature of 900 °C at a rate of 10 °C/s and then held for 300 s. Considering that the specimens in actual production process need to be transferred from the heating furnace to mold quickly, the temperature of the specimen was reduced to about 800 °C at 7 °C/s approximately, and then, the quenching process was simulated at the cooling rate of 45 °C/s by using the continuous annealing simulator (CCT-AY-II produced by Ulvac-Riko INC.). Finally, specimens were cooled in air to room temperature from 230 °C.
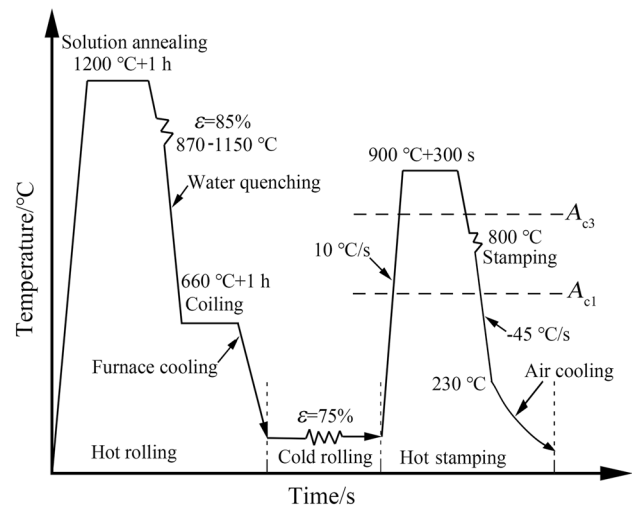

Fig. 1 Schematic diagram of hot-stamping process. ε Reduction rate

Table 1 Chemical composition and phase transition point of experimental steels

Steel	C/wt.%	Si/wt.%	Mn/wt.%	Al/wt.%	Cr/wt.%	B/wt.%	Ti/wt.%	Nb/wt.%	V/wt.%	A_{c1}/°C	A_{c3}/°C	M_s/°C	M_f/°C
V free	0.31	0.30	1.50	0.030	1.00	0.0020	0.070	0.046	–	732	789	349	149
0.14 V	0.31	0.27	1.48	0.030	1.01	0.0018	0.068	0.048	0.14	737	863	365	205

A_{c1} Austenite transformation starting temperature; A_{c3} austenite transformation finishing temperature; M_s martensite transformation starting temperature; M_f martensite transformation finishing temperature

2.2 Experimental procedures

Experiment I: hydrogen permeation test. The permeation curves, hydrogen diffusion coefficient (D_{ap}) and diffusion hydrogen concentration (C_0) were measured according to the modified ISO 17081 (2005) standard method in a Devanathane–Stachurski cell [20]. The specimens were mechanically polished to 2000-grit SiC emery paper on both sides. Furthermore, Watt's method was used to nickel (Ni) electroplate on the hydrogen expansion side. The nickel layer can not only protect the steel membrane against corrosion but also improve the transformation from hydrogen atoms (H) to hydrogen ions (H^+) as catalyst and be convenient for receiving current signal [21]. The aqueous solution in the hydrogen detection cell was 0.2 mol/L NaOH and in the hydrogen charging cell was 0.25 g/L CH_4N_4S and 0.5 mol/L H_2SO_4 mixed solution, in which the hydrogen charging current density was 1.0 mA/cm^2. A device schematic of the Devanathane–Stachurski setup is shown in Fig. 2a [20–22], and specimen dimension is shown in Fig. 2b.

Experiment II: slow strain rate test (SSRT). The experimental specimens used for SSRT were machined to meet the requirement of the uniaxial tensile test, while the shape and dimension of the specimen are shown in Fig. 2c. Prior to electrolytic pre-charged hydrogen, the gauge length of the tensile specimens was polished by up to 2000-grit SiC emery paper along the tensile direction to remove the oxides and ensure the same thickness of 1.5 mm and then cleaned with alcohol. Hydrogen was introduced into the specimens by electrochemical pre-charging in 0.1 mol/L NaOH aqueous solution at a current density of 5.0 mA/cm^2 for 24 h. Cadmium was immediately plated after hydrogen charging to prevent hydrogen from diffusing through specimens during subsequent tests. SSRT was then performed on a CMT5605 tensile test machine with a relatively low and constant strain rate of 10^{-5} s^{-1} in the air at room temperature.

The metallographic specimens of the steel plate were mechanically polished after quenching, and then the microstructure was observed using a ZEISS ULTRA 55 field emission scanning electron microscope after etching with 3 vol.% Nital. Electron backscatter diffraction (EBSD) measurement (step size: 0.15 μm; tilt angle: 70°) was carried out after electrolytic polishing in an electrolyte solution at ambient temperature (9 vol.% alcohol and 1 vol.% perchloric acid with a constant voltage at 15 V for 30 s). Finer microstructure in the steel was analyzed by JEM2100 transmission electron microscopy and the preparation process is as follows: the specimens after heat treatment were cut into 0.5 mm in thickness by electrical discharge machining and then reduced to 0.05–0.06 mm by mechanically thinning and finally conducted by double-spray treatment, with the double-spray solution of 5 vol.% of perchloric acid in ethanol, the voltage of 40–50 V, the current of 20–25 mA and the temperature of − 20 °C.
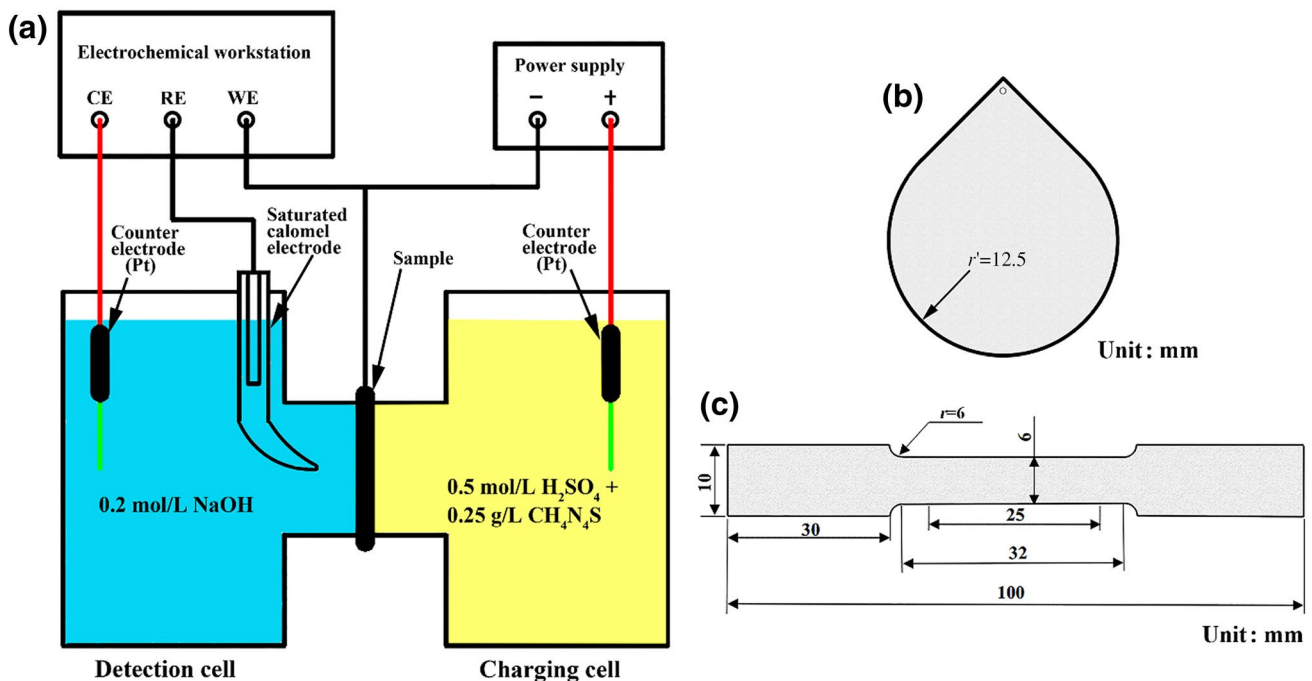

Fig. 2 Hydrogen permeation test device (**a**) and shape and dimension of specimens for hydrogen permeation test (**b**) and SSRT (**c**). CE, RE, WE and Pt represent counter electrode, reference electrode, working electrode and platinum wire, respectively
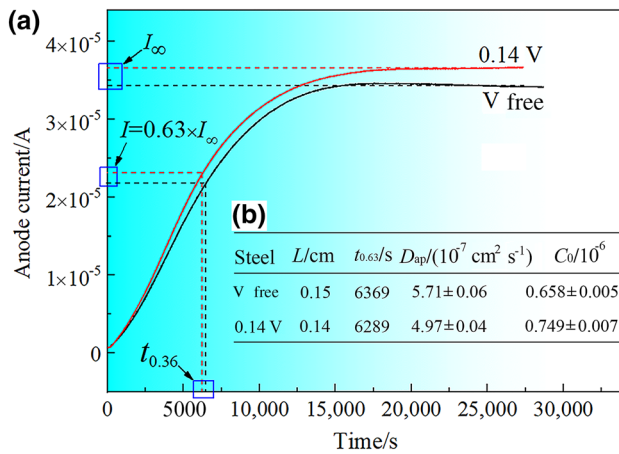
Fig. 3 Hydrogen permeation curves (**a**) and corresponding hydrogen permeation results (**b**) of V free and 0.14 V specimens

3 Results

3.1 Hydrogen diffusing behavior

Figure 3a shows the real-time changes in the current during the hydrogen permeation tests. Some physical parameters of the experimental steels could be obtained from the curves. The effective D_{ap} and C_0 are important parameters for characterizing HE susceptibility. D_{ap} and C_0 can be calculated as follows [23]:

$$D_{ap} = \frac{L^2}{6t_{0.63}} \tag{1}$$

$$C_0 = 1.31 \times 10^{-6} \frac{I_\infty L}{D_{ap} S} \tag{2}$$

where L is the thickness of the specimen, cm; I_∞ is the saturated current, A; S is the area exposed, cm^2; and $t_{0.63}$ is the time-lag at the instant when the current I was saturated to 0.63 of the steady-state current, s. The results are presented in Fig. 3b and demonstrated that D_{ap} in 0.14 V steel is lower than that in V free steel, while C_0 shows an opposite trend. It is illustrated that the hydrogen atoms in V free steel are more easily diffused and aggregated, and 0.14 V steel exhibits better resistance to HE.

3.2 Results of SSRT

The indexes (percentage of strength and plasticity reduction) are used for evaluating hydrogen embrittlement resistance ability (R), which are defined as [24]:

$$R = \frac{R_0 - R_5}{R_0} \times 100\% \tag{3}$$

where R_0 and R_5 represent the experimental parameters (such as fracture strength (FS) and total elongation) by SSRT in air after pre-charged hydrogen with the current density of 0 mA/cm^2 (the specimens were placed in 0.1 mol/L NaOH aqueous solution for 24 h without electricity) and 5.0 mA/cm^2 (the hydrogen charging environment remained consistent), respectively. Generally, the smaller the percentage of strength reduction, the better the resistance when confronting hydrogen embrittlement. Kong et al. [24] indicated that when $R \geq 35\%$, the material is HE with a high probability; when $25\% < R < 35\%$, HE may occur to material; $R \leq 25\%$ means that the material is immune to HE.

Stress–displacement curves of the steels obtained by SSRT in air after pre-charged hydrogen are shown in Fig. 4, from which we can infer that the uncharged specimen shows ductile fracture and obvious necking. When the hydrogen charging current density is 5.0 mA/cm^2, the experimental steel has no obvious necking and belongs to brittle fracture. The corresponding calculation results are also presented in Fig. 4. Percentage of fracture strength reduction (R_f) of V free steel and 0.14 V steels is 56.3% and 40.8%, and percentage of total elongation reduction (R_e) of V free steel and 0.14 V steel are 87.1% and 82.1%, respectively. Severe hydrogen embrittlement occurred in the experimental steels, and percentage of strength and plasticity reduction of 0.14 V steel is smaller than that of V free steel. It is concluded that the vanadium microalloying can effectively improve HE resistance of the high-strength hot-stamped steel. Rather remarkably, the fracture strength and total elongation of 0.14 V steel undergoing SSRT with 0 mA/cm^2 hydrogen
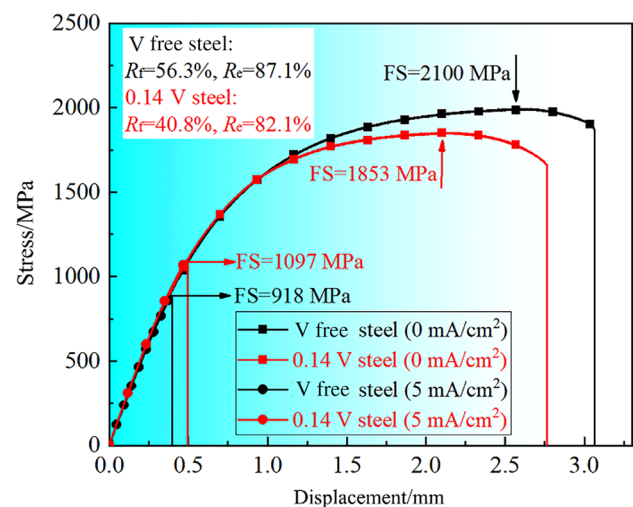

Fig. 4 Stress–displacement curves obtained and corresponding calculation results by SSRT of experimental steels

charging current density slightly decrease compared with those of V free steel. According to the previous research work [25, 26], vanadium and carbon have a strong binding energy, and the addition of V element consumes the carbon content in the experimental steel and reduces the martensitic strength and the volume fraction of retained austenite.

After SSRT, the specimen is immediately removed from the tension test machine, cleaned with alcohol and dried. The fracture surfaces analysis is conducted by ZEISS

ULTRA 55 scanning electron microscopy (SEM). Figure 5 shows the fracture morphology of the tests investigated. All uncharged specimens present typical ductile micro-void coalescence with dimples, as shown in Fig. 5a, b (magnified area marked by solid white line rectangle in Fig. 5a). Besides, the fracture surfaces of specimens by SSRT in air after pre-charged hydrogen are typical brittle fracture with a mixture of quasi-cleavage, transgranular and intergranular rupture [27, 28], as shown in Fig. 5c–f. For V free steel at
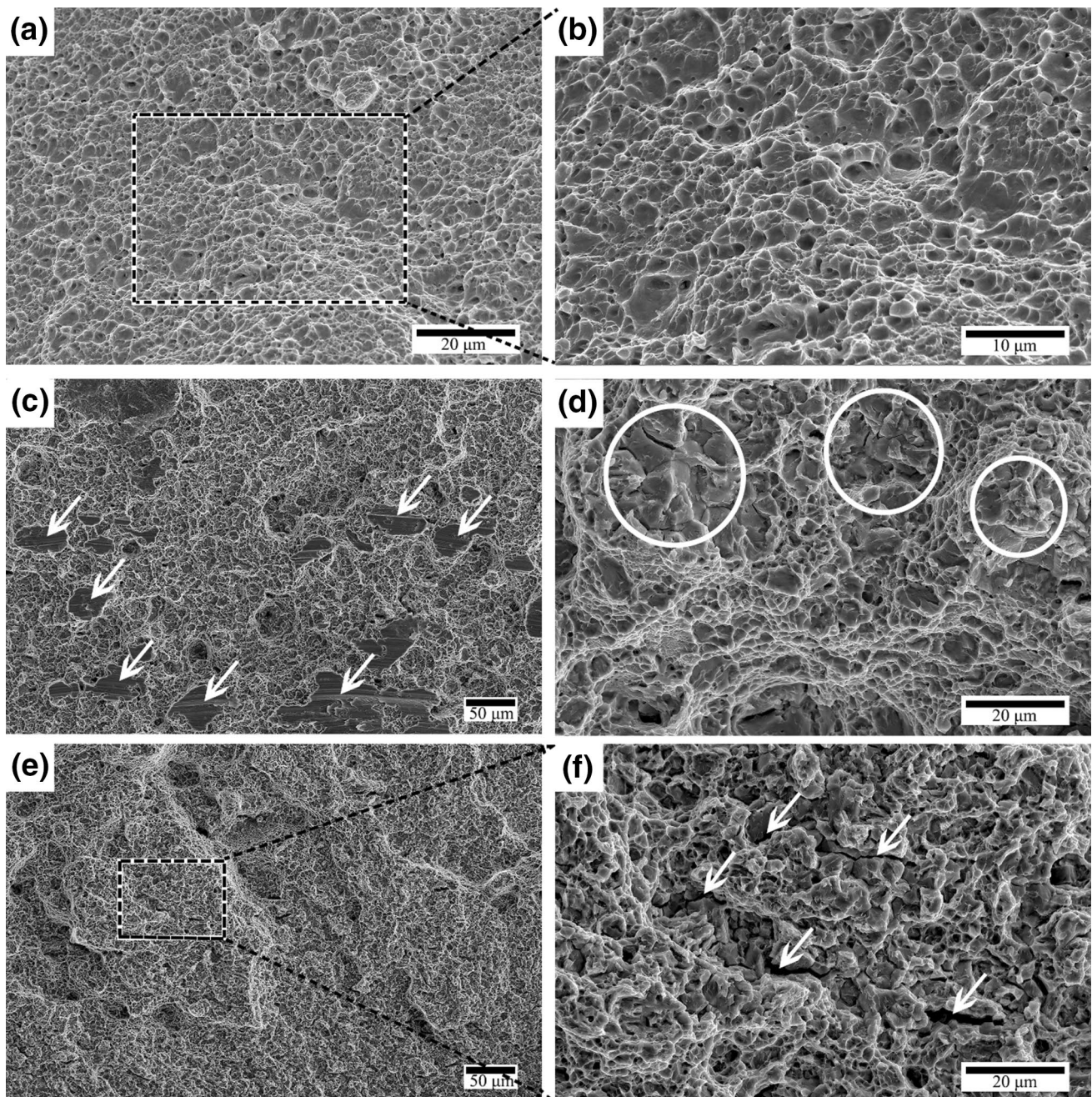

Fig. 5 SEM images of fracture morphologies in 0.14 V steel (**a**, **b**, **e**, **f**) and V free steel (**c**, **d**) in SSRT after pre-charged hydrogen with current density of 0 mA/cm^2 (**a**, **b**) and 5.0 mA/cm^2 (**c**–**f**)

5.0 mA/cm^2 hydrogen charging current density, the fracture surface is characterized by quasi-cleavage planes (Fig. 5c), intergranular fracture with rock candy shape (Fig. 5d) and very little dimples, indicating a high susceptibility to hydrogen embrittlement. For 0.14 V steel at 5.0 mA/cm^2 hydrogen charging current density, the dimples are slightly decreased (Fig. 5e), and some secondary cracks are observed as well (Fig. 5f). SEM fractographs show that the intergranular fracture, a typical characteristic of brittle fracture [13], more easily emerges and tends to be more serious in V free steel than in 0.14 V steel through analyzing pre-charged hydrogen fracture surface, and hence, the addition of V is beneficial to the improvement in hydrogen embrittlement. Moreover, previous studies [6, 10, 29, 30] indicated that intergranular fracture is an evidence of the hydrogen-enhanced decohesion mechanism, and it is found that Fig. 5d presents obvious intergranular fracture. Thus, the hydrogen-enhanced decohesion mechanism was one of the HE mechanisms in the experimental steels.

Generally, it is reported that hydrogen-induced cracking occurrence in steels is closely related with inclusion and microstructure [31]. The hydrogen diffuses into regions of high triaxial tensile stresses or to some microstructural areas that contain defects such as the inclusions and microvoids and becomes entrapped. When hydrogen pressure reaches a critical value, the crack will be initiated [32]. Furthermore, SEM images of the cross sections near fracture undergoing SSRT with 5.0 mA/cm^2 hydrogen charging current density are presented in Figs. 6 (V free steel) and 7 (0.14 V steel), which illustrate that the inclusions mainly included two types. MnS is ductile inclusions, with an elongated shape along the rolling direction (RD), as shown in Figs. 6c and 7c. Another type of inclusion is individually cubic (Nb, Ti)C and (Nb, V, Ti)C, as
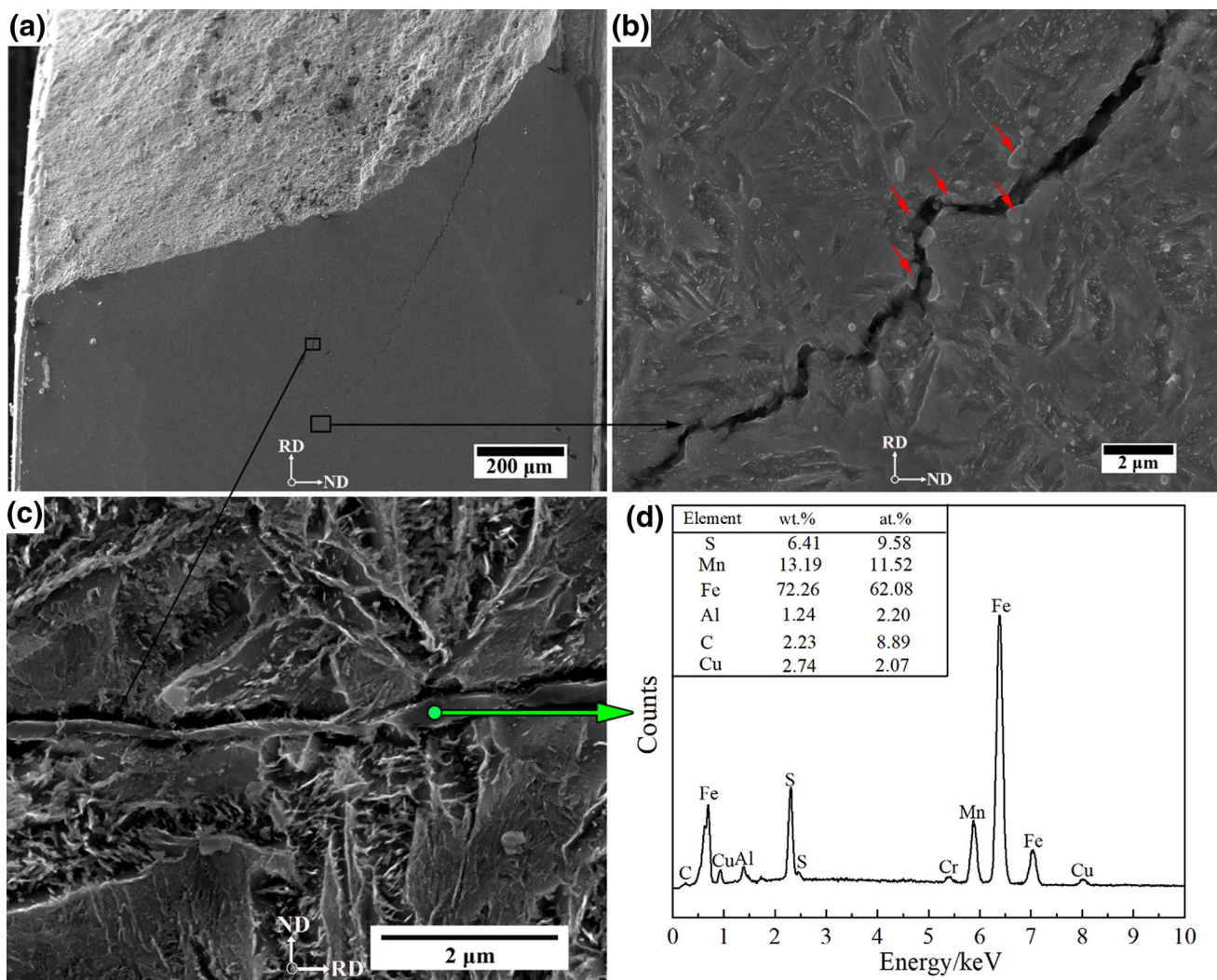

Fig. 6 SEM images of cross sections near fracture in V free steel. **a** Low magnification image of crack; **b** high magnified image of crack; **c** MnS inclusions; **d** energy dispersive X-ray (EDX) analysis result of inclusions in (**c**). ND Normal direction
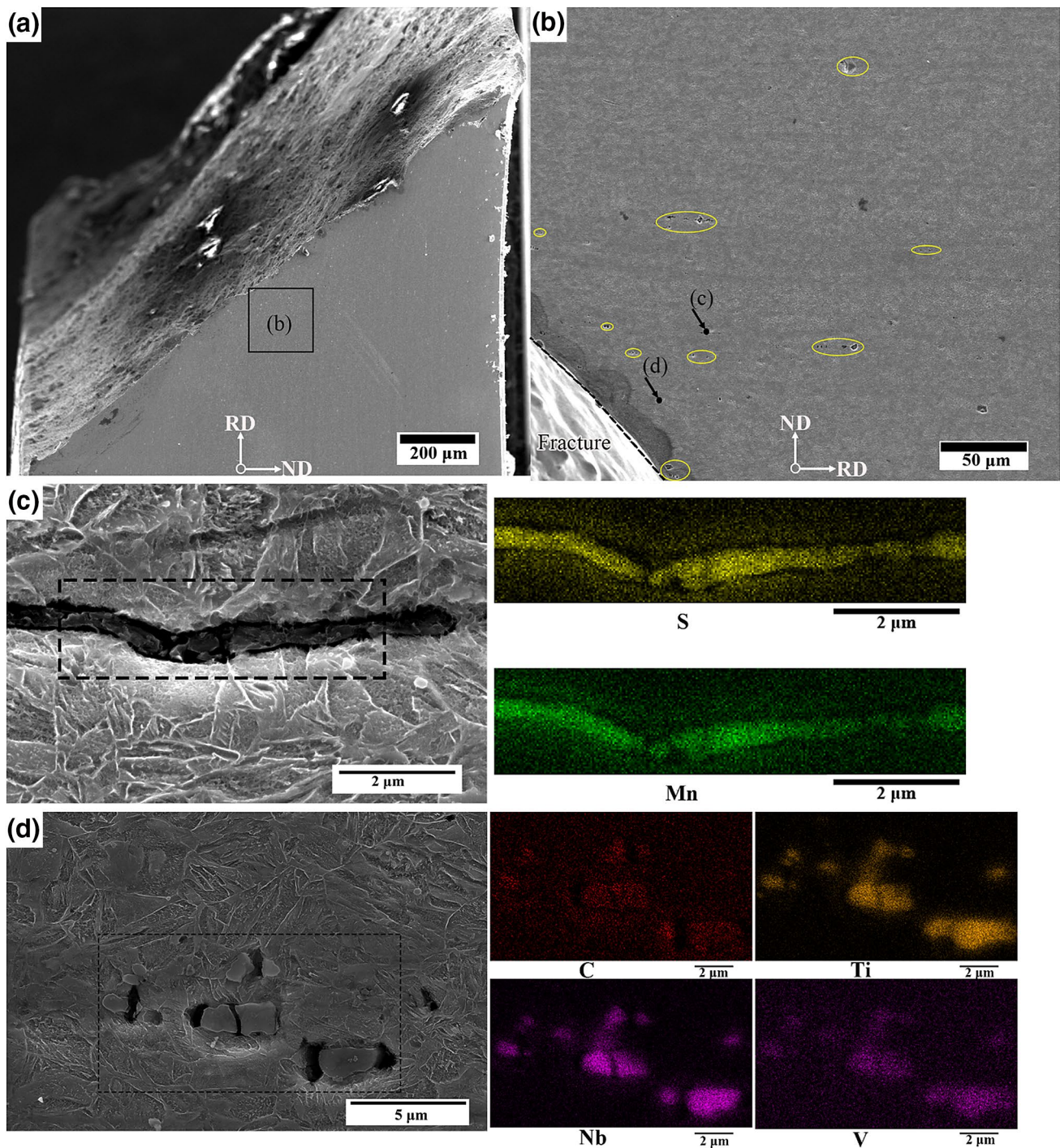
Fig. 7 SEM images of cross sections near fracture in 0.14 V steel. **a** Low magnification image; **b** high magnified image in (**a**); **c** MnS inclusions; **d** (Nb, V, Ti)C inclusions

shown in Figs. 6b (red arrow points) and 7d. Moreover, these inclusions are not well coherent to the steel matrix, and the interstice between inclusion and the matrix is clearly observed. It is worth mentioning that the coarse crack (Fig. 6a) is found in the V free steel after SSRT and the dominant direction of crack propagation is RD,

in which inclusions and microvoids are observed near crack propagation (Fig. 6b). Analogously, a large number of microvoids near fracture formed in 0.14 V steel are presented in Fig. 7b with yellow mark. Moreover, the types and distribution of inclusions are nearly the same in all the experimental steels. The reasons for the above

performance differences (as shown in Figs. 3, 4) between V free steel and 0.14 V steel will be discussed in the following contents.

3.3 Microstructural observations

EBSD micrographs showing the martensite structures of the V free steel and 0.14 V steel with the same heat treatment process are presented in Fig. 8. As known from Ref. [33], most of the boundaries created during the martensite transformation are either low-angle boundaries (< 15°) or high-angle boundaries in the range from 50° to 63°. In this paper, the boundaries with angle varying from 15° to 50° are added to martensite phase of bcc structure to extract the possible prior austenite grain boundaries. It is apparently illustrated that the prior austenite grains of 0.14 V steel (~ 3.6 ± 0.3 μm) are more uniform and finer than those of hot-stamped steel without V (~ 6.5 ± 0.4 μm), and the width

of martensite block in 0.14 V steel is smaller than that of V free steel as well.

Figures 9 and 10 show SEM and transmission electron microscopy (TEM) images of the experimental steels after quenching treatment. The microstructure of experimental steels consists of fresh martensite (FM) and tempered martensite (TM), and some carbides distributed around TM are presented in Fig. 9. TEM images reveal that the martensite exhibited a lath shape and contained a high density of dislocations within the subgrains, as shown in Fig. 10a, b. A large number of second-phase particles can be observed in experimental steels (Fig. 10c, e) by the carbon extraction replicas technique. Rather remarkably, compared with V free hot-stamped steel, the amount and density of particles are greater and their sizes are much finer in 0.14 V steel. The second-phase particles are mixed carbides of (Nb, Ti)C in V free steel and (Nb, V, Ti)C in 0.14 V steel, which could be concluded by EDX spectrum analysis (Fig. 10d, f).
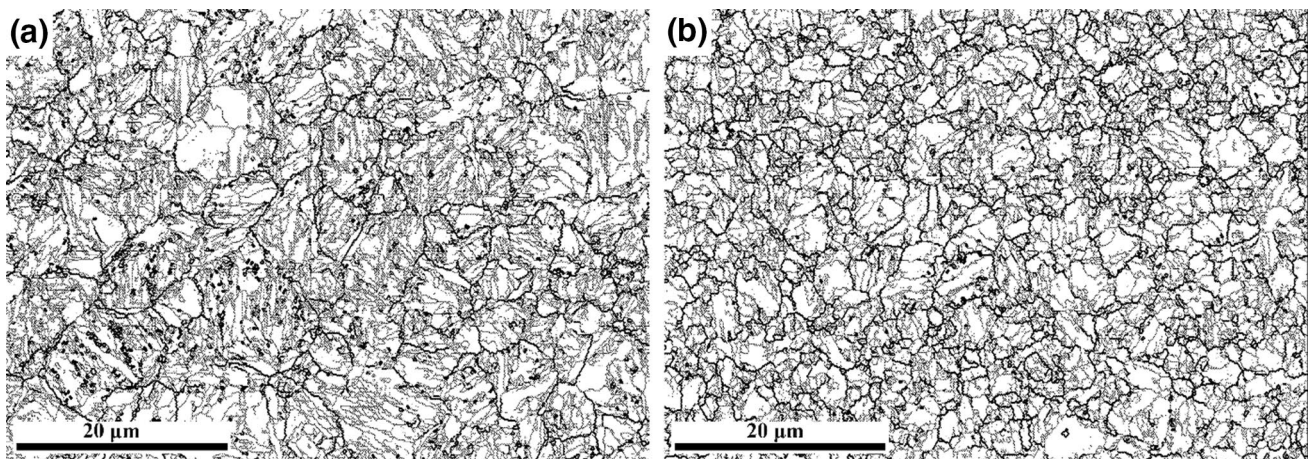

Fig. 8 EBSD microstructures of V free (**a**) and 0.14 V (**b**) specimens. Thick black lines and thin black lines indicate prior austenite grain boundary ($15° < \theta < 50°$) and martensite block grain boundary ($2° \leq \theta \leq 15°$ and $50° \leq \theta$), respectively

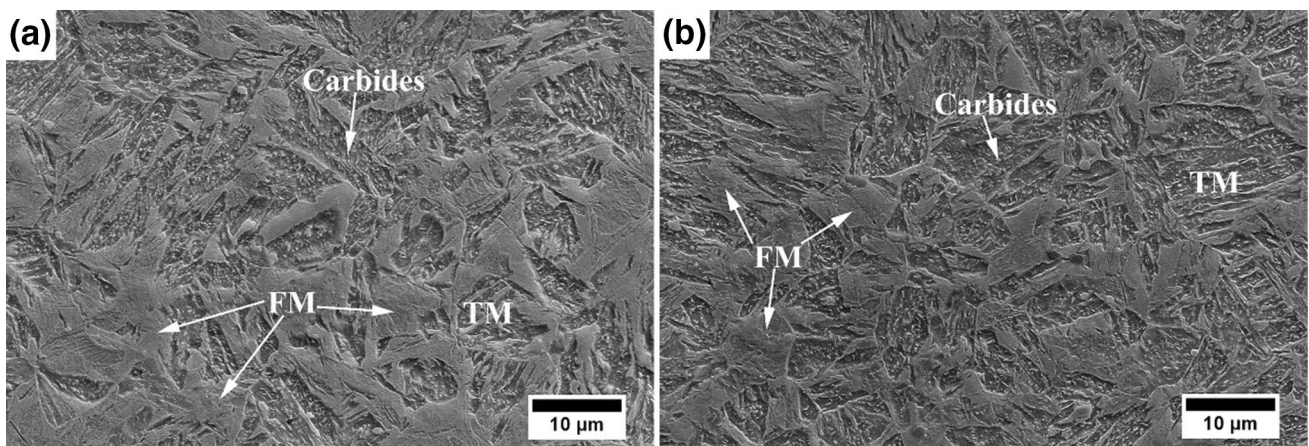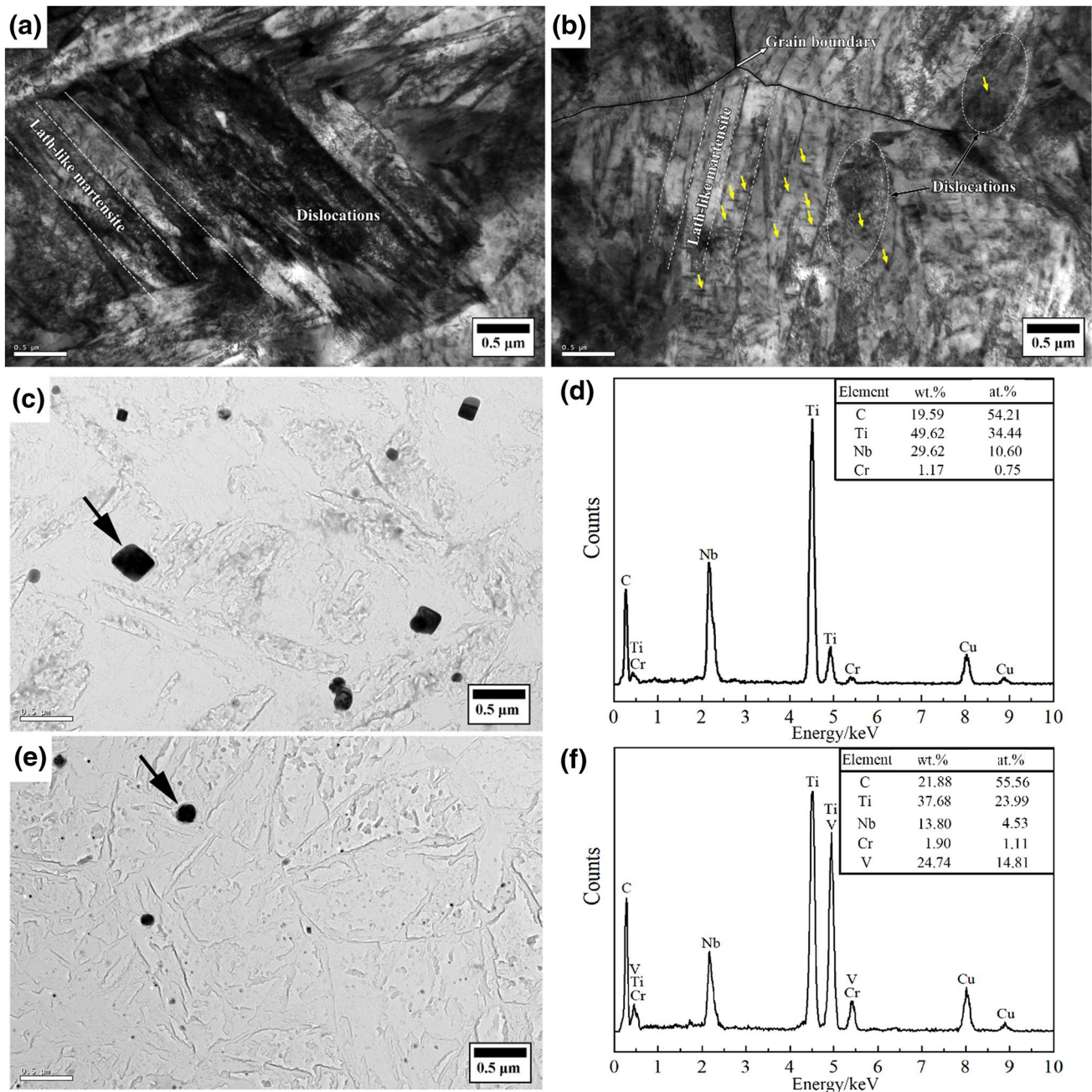**Fig. 9** SEM microstructure of experimental steels. **a** V free steel; **b** 0.14 V steel

Fig. 10 Martensite laths (**a**, **b**) and characteristic of precipitates (**c**, **e**) and EDX spectrum (**d**, **f**) in V free steel (**a**, **c**, **d**) and 0.14 V steel (**b**, **e**, **f**). Yellow arrows indicate second-phase particles

4 Discussion

4.1 Effects of vanadium in hot-stamped steels

The additions of microalloying elements in the experimental steel can notably improve its hardenability, and then full martensitic structures could be attained at much lower cooling rates, and Nb, V and Ti can form precipitates with C and N elements to strengthen the matrix. The phase fraction of V

carbides in 0.14 V hot-stamped steel and chemical element components in V carbides are calculated by Thermo-Calc software with database TCFE7 [34], as shown in Fig. 11a, b, respectively. It is illustrated that the peak precipitation temperature T_P and the dissolution temperature T_D of V carbides are 1014 and 1146 K, respectively.

According to the second-phase theory of steel [35], microalloying elements exist in the form of solid solution or precipitates, and their roles in steel are distinctly different,
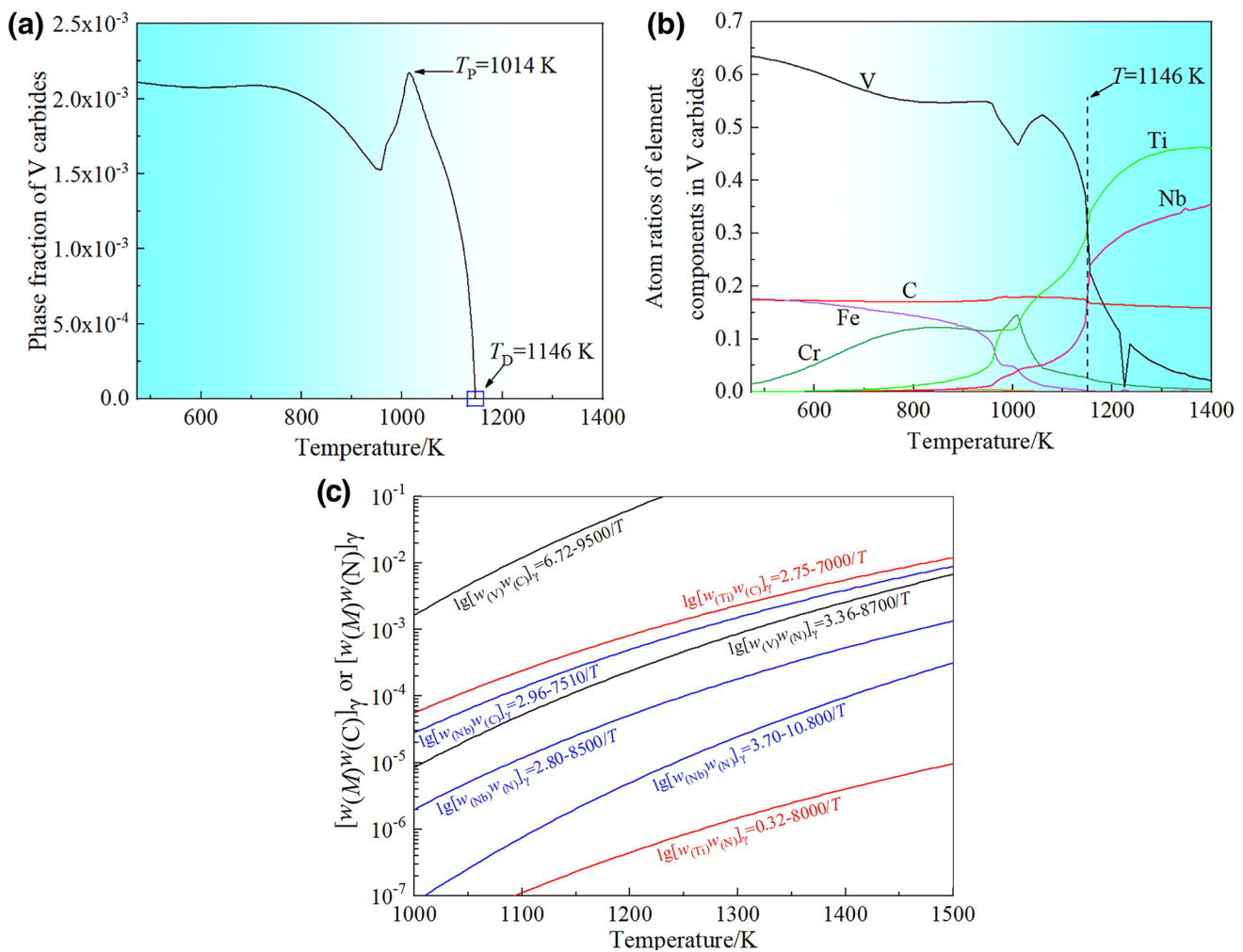
Fig. 11 Phase fraction (**a**) and chemical element components (**b**) of V carbides calculated by Thermal-Calc and TCFE7 database and comparison of solubility product formula of carbide or nitride for Nb, V and Ti in austenite (**c**). *T* Temperature

by comparing the second-phase solid solubility product formula, and thus determining its corresponding mechanism and degree of action. In this experimental steel, three kinds of microalloying elements of Nb, V and Ti are added, and the solid solubility product of the precipitates formed in the steel can be expressed by the following equation:

$$T_{AS} = \frac{B}{A - \lg\left[w_{(M)}w_{(X)}\right]} \tag{4}$$

where T_{AS} is the full solution temperature; A and B are constant; and $w_{(M)}$ and $w_{(X)}$ are the mass fraction of M and X elements in steel. According to Eq. (4), a comparison of the common solid solubility product formulas of the carbides or nitrides of niobium, vanadium and titanium in austenite (of which two formulas are given by NbN) is shown in Fig. 11c.

As shown in Fig. 11c, VC has a very high solid solubility product. If 0.31 wt.% C in steel is fully synthesized from

0.14 wt.% V junction with VC particles, the value of $w_{(V)}w_{(C)}$ is 0.04. The equilibrium solid solution value of VC is also 0.04 when the experimental steel is heated to 1173.15 K. According to the calculated value, if the vanadium-containing steel is kept at 1173.15 K for a long time, V in the steel should be in the form of solid solution atoms. However, during this experiment, we observe a large number of (Nb, V, Ti)C particles (Fig. 10e) in 0.14 V hot-stamped steel. Combined with the results obtained, it can be concluded that the grain boundary migration is hindered due to the combined actions of V solute atom dragging and VC precipitation pinning. Therefore, the grain of 0.14 V steel is significantly refined.

4.2 Precipitation and susceptibility to hydrogen embrittlement

The fundamental cause of hydrogen-induced delayed fracture in high-strength steels is the interaction between
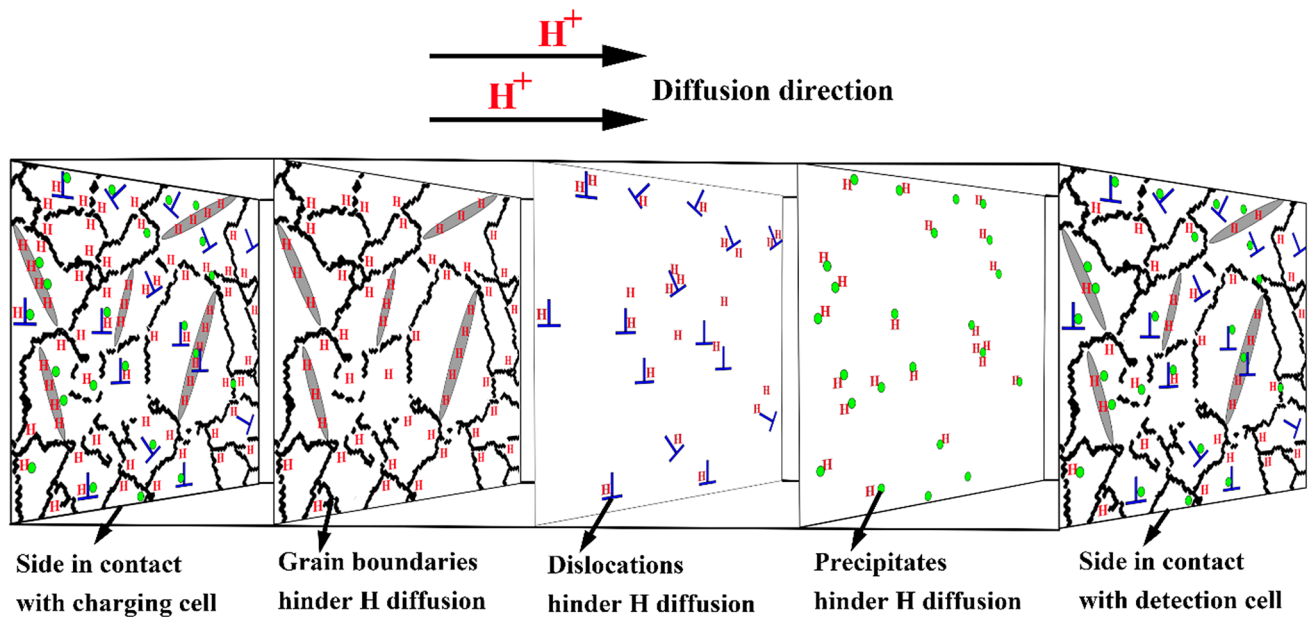
Fig. 12 Schematic of hydrogen diffusion in hydrogen permeation test

diffusible hydrogen and crystal defects including grain boundary and dislocation. As mentioned above, the hydrogen-induced cracking will occur when the enriched hydrogen content in the crystal defect exceeds its critical concentration. With the inability to control the hydrogen environment and external loading modes, reducing the hydrogen content in the steel is one of the most effective ways to improve its hydrogen embrittlement susceptibility [14].

In this study, based on the chemical composition of traditional hot-stamped steel (e.g., 22MnB5 and 30MnB5), we have designed 30MnBNbV steel which has potent resistance to HE through the above experimental results. The diffusion behavior of hydrogen in materials is mainly related to the number of grain boundaries [36, 37], precipitates [38] and dislocations [36, 38] that can become hydrogen traps. When there are more hydrogen traps inside the material, the diffusion of hydrogen will be more seriously hindered and can reduce the effective D_{ap} and increase C_0. Accordingly, the schematic of hydrogen diffusion during the hydrogen permeation test is presented in Fig. 12. The grain boundary and dislocation are reversible hydrogen trap [28], and combining microalloying elements (Nb, V and Ti) with C elements contributing to forming second-phase particles is irreversible hydrogen traps [39]. Compared to the V free experimental steel, the hydrogen traps in 0.14 V steel included not only inclusions and microvoids but also, more importantly, precipitates. 0.14 V steel has a large number of dispersive precipitates (Fig. 10e) and more grain boundary areas (Fig. 8b), which carry hydrogen atoms dispersedly distributed and not easily aggregated and diffused.

5 Conclusions

1. The diffusion coefficient of hydrogen and the percentage of strength and plasticity reduction in 0.14 V steel are lower than those in V free steel. Accordingly, 0.14 V hot-stamped steel has potent resistance to hydrogen embrittlement and ultra-high strength (≥ 1800 MPa) at the same time.
2. All uncharged hydrogen specimens present typical ductile fractures with a large number of dimples. Besides, the intergranular split and a standard characteristic of brittle fracture more easily emerge and tend to be more severe in V free steel than in 0.14 V steel through analyzing pre-charged hydrogen fracture surface.
3. 0.14 V hot-stamped steel has a large number of (Nb, V, Ti)C precipitates, which refine the microstructures and pin dislocations. Thereby, a lot of hydrogen traps are obtained, which hinder the diffusion and aggregation of hydrogen atoms.

References

[1] H. Karbasian, A.E. Tekkaya, J. Mater. Process. Technol. 210 (2010) 2103–2118.

[2] M. Merklein, M. Wieland, M. Lechner, S. Bruschi, A. Ghiotti, J. Mater. Process. Technol. 228 (2016) 11–24.

[3] M. Naderi, M. Ketabchi, M. Abbasi, W. Bleckb, J. Mater. Process. Technol. 211 (2011) 1117–1125.

[4] D.W. Fan, S.K. Han, B.C. De Cooman, Steel Res. Int. 80 (2009) 241–248.

[5] X.F. Li, J. Zhang, Y.F. Wang, B. Li, P. Zhang, X.L. Song, Mater. Sci. Eng. A 641 (2015) 45–53.

[6] M.B. Djukic, V.S. Zeravcic, G. Bakic, A. Sedmak, B. Rajicic, Procedia Mater. Sci. 3 (2014) 1167–1172.

[7] X.L. Zhao, Y.J. Zhang, W.J. Hui, C.Y. Wang, H. Dong, J. Iron Steel Res. 31 (2019) 837–847.

[8] X.F. Li, J. Zhang, S.C. Shen, Y.F. Wang, X.L. Song, Mater. Sci. Eng. A 682 (2017) 359–369.

[9] L. Jemblie, V. Olden, O.M. Akselsen, Int. J. Hydrogen Energy 42 (2017) 11980–11995.

[10] M. Koyama, C.C. Tasan, E. Akiyama, K. Tsuzaki, D. Raabe, Acta Mater. 70 (2014) 174–187.

[11] Y. Han, J.J. Shi, L. Xu, W.Q. Cao, H. Dong, Mater. Sci. Eng. A 530 (2011) 643–651.

[12] M.H. Cai, Z. Li, Q. Chao, P.D. Hodgson, Metall. Mater. Trans. A 45 (2014) 5624–5634.

[13] S.Q. Zhang, Y.H. Huang, B.T. Sun, Q.L. Liao, H.Z. Lu, B. Jian, H. Mohrbacher, W. Zhang, A.M. Guo, Y. Zhang, Mater. Sci. Eng. A 626 (2015) 136–143.

[14] Y.S. Chen, D. Haley, S.S.A. Gerstl, A.J. London, F. Sweeney, R.A. Wepf, W.M. Rainforth, P.A.J. Bagot, M.P. Moody, Science 355 (2017) 1196–1199.

[15] X.D. Tan, Y.B. Xu, X.L. Yang, Z.Q. Liu, D. Wu, Mater. Sci. Eng. A 594 (2014) 149–160.

[16] T.Y. Hsu, X.J. Jin, Y.H. Rong, J. Alloy. Compd. 577 (2013) S568–S571.

[17] A. Shibata, S. Daido, D. Terada, N. Tsuji, Mater. Trans. 54 (2013) 1570–1574.

[18] S.W. Seo, G.S. Jung, J.S. Lee, C.M. Bae, H.K.D.H. Bhadeshia, D.W. Suh, Mater. Sci. Technol. 31 (2015) 436–442.

[19] L.F. Lv, L.M. Fu, Y.L. Sun, A.D. Shan, Mater. Sci. Eng. A 731 (2018) 369–376.

[20] J. Li, J.S. Wu, Z.H. Wang, S.Q. Zhang, X.G. Wu, Y.H. Huang, X.G. Li, Int. J. Hydrogen Energy 42 (2017) 22175–22184.

[21] L.F. Li, B. Song, J. Cheng, Y.H. Yang, Z. Liu, Mater. Corros. 69 (2018) 590–600.

[22] L.F. Li, B. Song, J. Cheng, Z.B. Yang, Z.Y. Cai, Int. J. Hydrogen Energy 43 (2018) 17353–17363.

[23] S.Q. Zhang, E. Fan, J.F. Wan, J. Liu, Y.H. Huang, X.G. Li, Corros. Sci. 139 (2018) 83–96.

[24] D.J. Kong, Y.Z. Wu, D. Long, J. Iron Steel Res. Int. 20 (2013) No. 1, 40–46.

[25] G.W. Yang, X.J. Sun, Z.D. Li, X.X. Li, Q.L. Yong, Mater. Des. 50 (2013) 102–107.

[26] W.J. Chen, S. Wang, Z.Z. Zhao, J.T. Liang, J. Guo, J. Mater. Res. Express 6 (2019) 1065e3.

[27] X. Zhu, W. Li, H.S. Zhao, L. Wang, X.J. Jin, Int. J. Hydrogen Energy 39 (2014) 13031–13040.

[28] M.L. Martin, J.A. Fenske, G.S. Liu, P. Sofronis, I.M. Robertson, Acta Mater. 59 (2011) 1601–1606.

[29] X.F. Li, J. Zhang, E. Akiyama, Y.F. Wang, Q.Z. Li, Int. J. Hydrogen Energy 43 (2018) 17898–17911.

[30] B.S. Kumar, V. Kain, M. Singh, B. Vishwanadh, Mater. Sci. Eng. A 700 (2017) 140–151.

[31] W.K. Kim, S.U. Koh, B.Y. Yang, K.Y. Kim, Corros. Sci. 50 (2008) 3336–3342.

[32] E. Lunarska, Y. Ososkov, Y. Jagodzinsky, Int. J. Hydrogen Energy 22 (1997) 279–284.

[33] Z.Z. Zhao, J.T. Liang, A.M. Zhao, J.H. Liang, D. Tang, Y.P. Gao, J. Alloy. Compd. 691 (2017) 51–59.

[34] F. Peng, Y.B. Xu, X.L. Gu, Y. Wang, X.D. Liu, J.P. Li, Mater. Sci. Eng. A 723 (2018) 247–258.

[35] Q.L. Yong, Secondary phase in the steel, Metallurgical Industry Press, Beijing, China, 2006.

[36] K. Takasawa, R. Ikeda, N. Ishikawa, R. Ishigaki, Int. J. Hydrogen Energy 37 (2012) 2669–2675.

[37] S. Bechtle, M. Kumar, B.P. Somerday, M. Launey, R.O. Ritchie, Acta Mater. 57 (2009) 4148–4157.

[38] B.A. Szost, R.H. Vegter, P.E.J. Rivera-Díaz-del-Castillo, Mater. Des. 43 (2013) 499–506.

[39] A.J. Haq, K. Muzaka, D.P. Dunne, A. Calka, E.V. Pereloma, Int. J. Hydrogen Energy 38 (2013) 2544–2556.